РОССИЙСКАЯ АКАДЕМИЯ НАУК
ИНСТИТУТ ЯДЕРНЫХ ИССЛЕДОВАНИЙ

RUSSIAN ACADEMY OF SCIENCES
INSTITUTE FOR NUCLEAR RESEARCH

PREPRINT INR – 769/92
JULY 1992

A.B.Kurepin, V.A.Krasnov, Yu.K.Gavrilov, M.A.Prokhvatilov, M.B.Golubeva, V.I.Kopylov, V.A.Gladyshev, A.L.Proskuryakov, N.S.Topilskaya, V.I.Rasin, D.I.Zaikin, T.A.Golubeva, S.N.Philippov

Institute for Nuclear Research, Russian Academy of Sciences

O.O.Patarakin, A.A.Kartamyshev, V.I.Kovinski, S.A.Korobko, V.A.Danilov, K.N.Mukhin, A.F.Sustavov, V.V.Suslin, V.E.Keilin, I.A.Kovalev, V.A.Bol'shakov

I.V.Kurchatov Institute of Atomic Energy

A.A.Andrianov, G.A.Feofilov, V.V.Vereshagin, A.A.Bolokhov, F.F.Valiev, T.A.Tulina, V.M.Vinogrdov

St.Petersburg University

Spectrometer AMPIR for Investigation of Rare and Multiparticle Processes

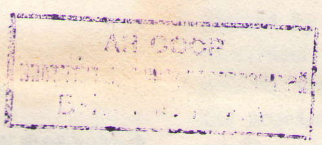

117312, Москва, проспект 60-летия Октября,7а
Институт ядерных исследований Российской академии наук

Institute for Nuclear Research of the Russian Academy of Sciences
60-the October Anniversary prospect 7a, Moscow 117312, Russia

INTRODUCTION

Production of intense π-meson beams [1] makes it possible to plan essentially new investigations of rare nuclear processes for the purpose of studying the non-nucleon degrees of freedom. Importance of these investigations is determined by the necessity of further progress in understanding nuclear structure and nuclear forces in the framework of the "traditional" meson and other theories as well as in terms of quantum chromodinamics. For successful development of both directions it is necessary to study experimentally the quark, meson, Δ – isobar and other nuclear substructures. Such a study is difficult in standard experiments, because of a smallness of corresponding effects, and needs specific conditions: high–intensity, good–quality beams and highly–sensitive detectors with good resolution.

Medium–energy pions and photons are most suitable evidently for using as primary particles. This is explained by unique properties of pions and photons as test particles: quantum numbers convenient for analysis, a variety of pion–nuclear and photon–nuclear reactions, and different types of pion and photon interaction with nucleons and nuclear clusters. The pion beams of high intensity (up to 10^8 π/s with an energy of up to 0.4 GeV to be produced at the Moscow meson factory (MMF).

Implementation of the physical program for investigation of rare pion–nuclear, proton–nuclear and photon–nuclear reactions needs a new–generation detector suitable for exclusive experiments. Such a detector must have fast response and ability of simultaneous recording and identification of several charged and neutral particles in a large solid angle with good spatial and energy resolution. The above requirements are met by a magnetic spectrometer AMPIR developed by the collaboration of I.V.Kurchatov Institute, Institute for Nuclear research of the Russia Academy of Sciences and Research Institute of Phisics of the St.Petersburg State University. The schematic layout of the spectrometer and the features of its use are presented in [3–5]. Below the physical program for investigation of rare and multiparticle processes as well as the spectrometer AMPIR are described.

1. Physical program

A. Pion–buclear experiments

1.1. Study of the $\pi N \to \pi\pi N$ reaction near threshold

Acquirement of reliable experimental data on production of pions by pions on protons has recently gained in importance. Interest in these data increased because of development of the chiral models, in particular the Scirm model [6]. To make the parameters of the theory more precise and to develop it further it is necessary to refine the $\pi\pi$– scattering phases shifts in the 280–500–MeV range of π–meson masses. Extraction of new data on the $\pi\pi$–scattering represents a difficult problem [7]. The traditional Chow–Low extrapolation to the pion pole requires that the single–pion exchange diagram would be dominant and, therefore, its tolerable kinematic region is limited to the 4π– vertex resonance region. To receive the information about the $\pi\pi$–interaction beyond the $\pi\pi$–resonance region the combined action of other mechanisms of the $\pi N \to \pi\pi N$ reaction should be apparently taken into account, which is essentially a multiparameter problem. The method developed in [8] makes it possible to determine accurately an appropriate minimum set of parameters and to formulate criteria for data processing. The combination of the traditional extrapolations to the pion pole with the practice of working in the physical range as well as the use of the Roy equations, provided the reliable experimental data with rich statistics are available, will allow a considerable progress in the understanding of this issue.

1.2. Study of the pion production by pions on nuclei

It should be noted that this process in the final state is evidently selective to the excitation of the nuclear levels with the pion quantum numbers. The calculations made under the momentum assumption with distorted waves for single–nucleon production showed that the cross–sections for excitation of discrete levels are very small (about several nbarn/MeV) [9]. Investigations of such states representing the spin–isospin excitations of nuclei are one of the basics. This is explained by the possible collective character of these states as in the case of the known Gamow–Teller 1+–resonance. Moreover it is expected that because of the precritical effects of pion condensation in nuclear matter the cross-section for the $(\pi, 2\pi)$ reaction on nuclei can increase at certain values of the transfer momentum [9]. These investigations have acquired a special actuality now since the effect of pion yield enhancement was found in [10] for events with small energy transferred to a nucleus at a transfer momentum of avout 250 MeV/c in the $(\pi, 2\pi)$ reaction on Fe and Ti nuclei. This enhancement is explained by the authors as a possible evidence of either precritical phenomena or existence of highly excited nuclear states. Seemingly, of essential interest is also the acquirement of data from the $(\pi^+, \pi^+\pi^0)$ and $(\pi^-, \pi^-\pi^0)$ reactions which can be attractive because of the absence of coulomb interaction of low–energy π^0–mesons near threshold. Such data are unavailable now.

1.3. Reactions of single charge exchange on nuclei

The reactions of pion single charge exchange are used to investigate the excitations of the isobar analog states in nuclei. The reaction cross–sections are small, (about a microbarn per steradian) and the number of measurements is limited. A wide range of measurements at various angles and energies with a variety of targets are required. The available experimental data are reviewed, for example, in [11].

The connection of the spin–isospin excitations in nuclear matter with the delta–isobar states excited in the reaction of pion charge exchange on nuclei is widely discussed. The first results for the (π^+, π^0) reaction on ^{12}C and Al were obtained in [12]; the 50 MeV shift of the Δ–isobar peak to lower excitation energies and its considerable broadening were observed. This is of special importance, because in this reaction the π–exchange is forbidden and the other diagrams, for examples ρ–meson exchange diagram, dominates. The agreement between the data obtained and the results extracted from other processes indicates that the shift depends on the properties of the Δ–isobar in the nucleus, rather than on the concrete mechanism of the reaction. However, high–resolution correlation measurements are required to understand the possible collectivity of these states.

1.4. Reaction of double charge exchange on nuclei

Excitation of the double–analog states of the target nuclei is the basic channel of this reaction. When analyzing the experimental data according to the two–step pion–nucleon mechanism, the values calculated at a pion energy of 50 MeV seemed to be essentially underestimated. This results from the smallness of the elementary $\pi^- p \to \pi^0 n$ cross–section. The attempt to introduce 6% of the impurity six–quark component into the wave function of a valence neutron was one of explanations [13]. More complete measurements are required to solve the problem.

1.5. Study of the few–nucleon systems

The setup having almost 4π geometry is required to carry out the kinematically complete experiments of the $\pi^+ d \to \pi^+ pn$, $\pi^+ d \to \pi^0 pp$ and other types. To study the production of nucleon resonances and their interaction with nucleons in nuclei it is necessary to increase the accuracy of measurement and the number of parameters to be measured. Measurements of such a kind must be made on nuclear targets where the narrow anomalies about 10 meV in width observed at dibarion masses of abour 2 GeV can be interpreted as hidden color states [14].

1.6. Search of exotic nuclei

Some pion reactions in nuclei can be used to produce exotic nuclei, such as ^{10}He, ^{15}B and ^{22}O, for example, the $(\pi^-, \pi^+ p)$ reaction on the ^{11}B, ^{16}O and ^{23}Na targets. Data on the pion reactions in nuclei on targets from rare isotopes or even on radioactive targets could be obtained with a high–efficiency setup.

B. Proton–nuclear experiments.

1.7. Study of the pion production by proton beams

In the last years the experimental study of the pion production by proton beams with resonably good energy resolution of the order 10^{-3} on nucleous and nuclei has a great importance. The interest in these date increased becouse of discovering of the anomalous pion production, investigated in the work [15]. However complete experiment for pion production with high energy resolution and polarization measurements should be done.

Measurements with polarized proton beam with identification of excited nuclear study can be used for investigation of the high momentum nucleon distribution in nuclei and for the study of the nature of the anomalous production. The problem of narrow dibaryon resonances could be also investigated.

The simultaneous detection of several particles can produce new date of dibaryon resonances and on of–shell effects in pion production data in nucleon–nucleon and nucleon–nuclear–interactions.

1.8. Nucleon–nuclear interactions.

The measuremant of spectra and polarization characteristics in (p, p), (p, n) and (n, p) reactions on nuclei in the wide kinematical range with simultaneous detection of several particles can reveal new information about non–nucleonic degrees of freedom in nuclei. For example in inclusive experiment for nucleon charge exchange reaction (p, n) the Δ–isobar excitation with energy about 300 Mev was observed. The shift was seen of Δ–isobar resonance down in the excitation energy scale from the excitation of the Δ–isobar in the reaction with hydrogen [16]. The correlation measurements with high energy resolution provide investigations of spin–isospin excitations in nuclei and the study of production, decay and absorption of the Δ–resonance in nuclei.

C. Photonuclear experiments.

The transparency of a nucleous for photons and the relative simplicity of the theoretical interpretation of electromagnetic processes allow one to hope for acquirement of new information about the mechanisms of the photonuclear reactions, the role of the non–nucleon degrees of freedom (delta–isobar, pion, quark, etc.), the specific behaviour of nucleon–nucleon cor-

relations at short distances, etc. We shall list some concrete investigations which can be set up with tagged photon beams and the spectrometer AMPIR.

1.9. Photoexcitation of the nuclear Δ–isobar.

The properties of the nuclear Δ–isobar are studied mainly in the processes of nucleon, pion and ion charge exchange, as a rule, in the inclusive experiments. Both circumstances impede the interpretation of results. It seems probable that these difficulties can be overcome in the exclusive experiment on production of a nuclear Δ–isobar in the electromagnetic process with recording the products of its decay and γ–rays from the excited final nucleus. It is planned to investigate the photoproduction of three components of an iso–quartet Δ–isobar on various nuclei in the $\gamma + A \to \Delta + A$ reactions with the decay pions and protons being recorded (the Δ^-–component cannot be studied in the exclusive variant because of the absence of a neutron detector in the spectrometer). The simultaneous investigation of the nuclear Δ^0, Δ^+ and Δ^{++} isobars could yield the information about the features of the Δ–isobar production in a nucleus and, in particular, in the nuclear interior, the passage of the isobar through the nucleus and its interaction with nuclear matter. It is possible to estimate the change in the Δ–isobar photoproduction amplitude in nuclear medium and to compare the results with the hole models.

1.10. Photon–deuteron interaction

It is seen from the structure of the final states in the $\gamma' d \to pp\pi^-$, $\gamma d \to d\pi^+\pi^-$ and $\gamma d \to pp\pi^0\pi^-$ reactions that their investigation can give information about the $N\Delta$ – and $\Delta\Delta$ – interaction, the passage of the Δ isobar through light nuclei and the isobar contribution to the deutron wave function.

1.11. Photon–helium interaction

A great number of reactions can be studied with a helium target the feasibility of which is discussed today. These are, for example, the $\gamma^4\mathrm{He} \to {}^4\mathrm{He}\pi^- p$, $\gamma^4\mathrm{He} \to d\pi^- pp$; $\gamma^4\mathrm{He} \to t\pi^0 p$ reactions. In addition to the above mentioned information about the spectific nature of the Δ–excitation of a light nucleus here there is every reason both to hope to obtain data on nucleon–nucleon correlation at short distances and to attempt to observe the dibaryon states.

1.12. Rare decays of an η--meson

Besides the evident reference reactions, such as $\gamma p \to p\pi^+\pi^-$ and $\gamma p \to p\pi^0$, the use of a liquid hydrogen target allows one to investigate the rare decays of an η–meson in the $\gamma p \to p\eta$ reaction. Results of this investigation are also interesting from the viewpoint of both their comparison with the results for the analogous reactions of η–meson photoproduction on nuclei to obtain information about the cross–section for photoproduction of an η–meson on a neutron and study of the multi-particle final states. The exact data on the cross–sections for such processes are required for comparison with the theoretical calculations. According to data of [15] the cross–section for the $\gamma d \to d\eta$ reaction near threshold differs from the theoretical one by a factor of 2.5.

1.13. Photoproduction of oppositely charged pion pairs

The $\gamma + A \to \pi^+ + \pi^- + A'$ process is often named the Compton effect on a π–meson. At low energies $E_\gamma \lesssim$ 1 GeV the reaction is governed by both electromagnetic and strong interactions. This holds out the hope of receiving the information about the ππ – interaction with taking account of the π–meson rescattering. The preliminary estimation shows that the total reaction cross–section is 100–500 nbarn and the contribution to the cross–section from the pion rescattering can be 10–20%. To analyze the results of the investigation of this reaction it is possible to use the theory of broken chiral symmetry of strong interactions [16] that were successfully used to extract the information about the ππ–scattering from such reactions as $\pi N \to \pi\pi N$.

2. Design of the AMPIR spectrometer

2.1. Spectrometer lay–out

The lay–out of the spectrometer is shown in Fig.1. Its basic components are: target 1, vacuum tube 2 with an insertion "transparent" to particles near the target, vertex detector 3, internal cylingrical drift chamber 4 and large-volume external drift chamber 5 to detect charged particles, trigger scintillation counters with optical fibres 6, superconducting solenoid 7, neutral–particle detector 8, sectional profiled iron magnetic–yoke 9, input unit 10 to supply power and cryogenic coolants into the spectrometer and leak–tight tank 11. In designing the authors started from the necessity to ensure the following parameters of the spectrometer:

1. Reliable identification and high accuracy in determining the momentum of charged particles ($\Delta p/p \cong$ 0.01 – 0.02) up to 1000 MeV/c;

2. High recording efficiency (≅ 14 rediation lengths) for gamma-rays and π^0–meson at good resolution (≅ 5%);

3. Capability to record simultaneously 2 to 8 charged particles with an energy $E \geqslant 20$ MeV and up to 6 γ-rays (2–3– mesons) with energies $E\gamma \geqslant 3$ MeV and $E_{\pi^0} > 0$;

4. Large solid angle of particle detection ($3\pi < \Omega < 4\pi$);

5. Capability to work with various solid and cryogenic targets;

6. High accuracy in determining the vertex of interaction inside the target;

7. Fast electronics slowing the operation with the highintensity ($\cong 10^8$ s^{-1}) beams of primary particles, i.e. the recording of rare events with σ = 1–10 nbarn.

The individual components of the spectrometer and their current status are described below.

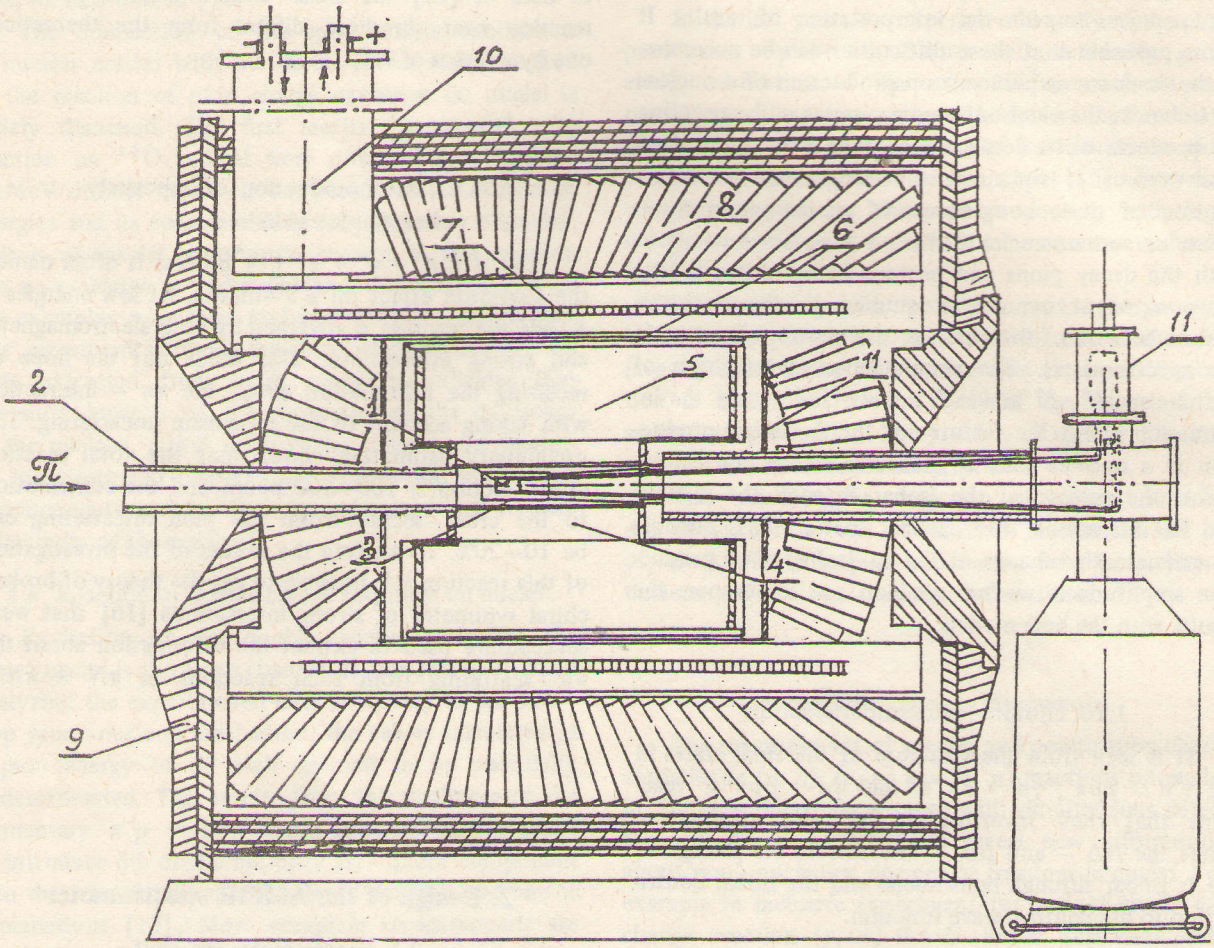

Fig. 1. The lay–out of the AMPOR spectrometer: 1 – target; 2 – vacuum tube; 3 – vertex detector; 4 – internal drift chamber; 5 – 100-cm–long drift chamber; 6 – scintillators; 7 – coil of superconducting solenoid; 8 – neutral particle detector; 9 – magnetic yoke; 10 – cryostat.

2.2. Superconducting magnet

The superconducting radiation–transparent solenoid with an iron magnetic yoke produces at a current of 2.8 kA a magnetic field of 10 kG with a nonuniformity of about 2% in the working volume 0.9 m in deameter and 1 m long.

The solenoid is composed of a selt–supported two–layer edgewise coil made of a superconducting 7x4 – mm^2 bar (a twist from 8 metal–matrix–composite niobium–titanium wires CKHT–0.7–210–0.5 soldered in a rectangular slot in the middle part of a bimetallic aluminium–copper bar). The bar is insulated by 0.2–mm–thick cotton cloth.

The length of the solenoid is 1800 mm (410 turns per layer), its inner diameter is 1144 mm. The energy stored in a magnetic field of 10 kG is about 0.74 MJ.

The method of indirect cryostating is used to cool the solenoid. Liquid helium is fed through inlet headers, flows inside 24 parallel thin–walled aluminium 12–mm–diameter pipes fixed with an epoxy adhesive on the outer and inner surfaces of the coil and is collected in outlet headers.

The thermal insulation of the solenoid consists of socalled mylar blanket made up to several tens of superinsulation layers (10–μm–tick mylar metallized with aluminium on a special biberglass base), a soft nitrogen

screen shipped with aluminium pipes with liquid nitrogen, and the second mylar–blanket superinsulation. The outer and inner shells of the cryostat are made of aluminium alloys (Fig. 2).

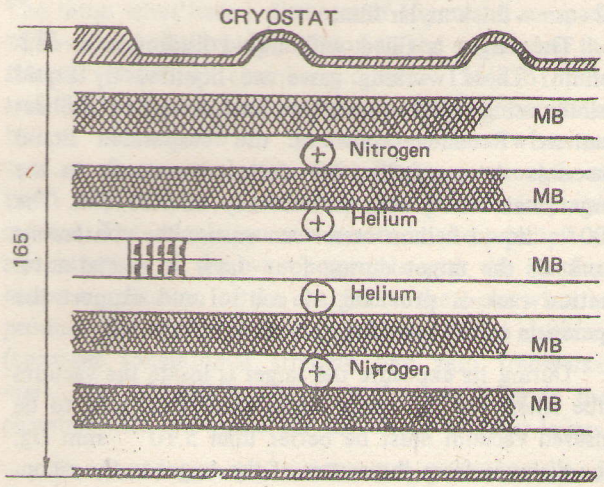

Fig. 2. The schematic of the superconducting solenoid cryostat

To compensate axial and radial forces arising in the magnetic field between the solenoid and the magnetic core poles the solenoid is suspended inside a cryostat by means of fiberglass composite laminate tension members and supports. The cryostat itself is attached to the frame plates of the magnetic core.

The developed designs of the solenoid and the cryostat have a very low absorptivity for γ-rays (0.4 of radiation length).

The 30-t magnetic yoke built up from 11 longitudinal plates and 2 end disks made of CT–10 steel is placed on an alignment base ensuring the positioning and correction of the magnet. The overall dimensions of the magnet are 3350 mm long, 2750 mm high and 2500 mm wide.

The special input unit with electric current leads and a 20–30 *l* liquid helium tank insulated from external heat by a superinsulation and a nitrogen screen is provided to supply electric power and liquid coolants to the spectrometer. The tank encloses a coil pipe into which liquid helium is pumped to cool the solenoid, and the superconducting sections of the lead conductors. The ends of the conductors soldered to the current leads are cooled with helium from the outlet heads. The helium temperature is 4.6°K at the inlet of the magnet coil 4.7°K at its outlet and no higher that 5.0°K in the "warmest" part. During the primary cooling the intake of liquid helium is provided by bypassing the input unit.

The expected distribution of the magnetic field along the solenoid axis and radius were confirmed by the calculations on the POISSON program for the described design and the simulation experiments at a 1:3 scale "warm" model magnet. It follows from these calculations and measurements that the magnetic field nonuniformity can attain 4–5% at the solenoid ends, but not exceed 2% in the working volume of the detector (l=1 m, d=0.9m).

The functional test of the solenoid was made with a 1:3 scale superconducting magnet having a coil shown in Fig. 3.

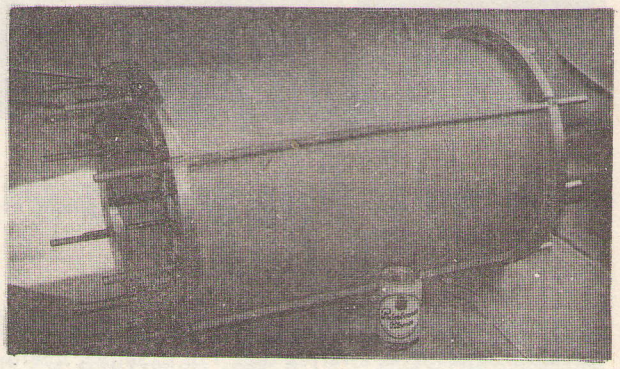

Fig. 3. The coil of the model superconducting solenoid.

2.3. Vacuum tube, target and vertex detector

The vacuum tube enclosing the target and the vertex strip detector in mounted along the solenoid axis and represents a separate leak–tight structure consisting of several sections made of non–magnetic materials. The entrance part equipped with a gate is connected to a ion guide of a pion, proton or photon channel of an accelerator; the central 80-mm-dia part of the vacuum tube (transparent to the reaction products) is made of 700 – m-thick carbon fiber reinforced plastic and connected with the entrance and exit parts by two belows. The exit part of the ion guide is designed to attach the vertex detector, to accommodate its preamplifiers together with cooling pipes and to connect a holder of a cryogenic or solid targets and a beam monitor.

The vertex detector holder represents a light tubular structure on which six paired 60x30–mm^2 silicon plates 300 m in thickness with longitudinal strips may be mounted (Fig. 4). The slices are attached to glass–cloth–base–laminate frames placed along the beam axis on the generatrices of a 60-mm-dia cylinder. Each slice represents an n-type silicon single crystal with 72 longitudinal p^+–strips 450 m in width ion-implanted in the single crystal surface with a spacing of 500 m. The signal appearing on the strip when a charged particle passes through the slice is supplied to the input of a semiconductor charge-sensitive preamplifier prepared by the hydrid technology. The coordinate of a particle is determined by the triggered channel number and its passage time is established from the pulse arrival moment.

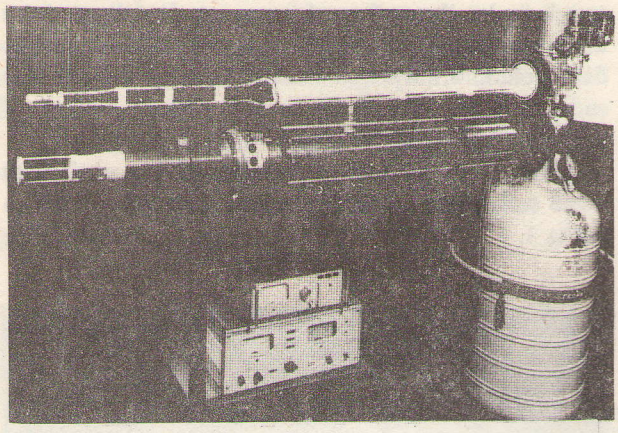

Fig. 4. The liquid–hydrogen target and the attachment of the vertex detector.

Other variants are also possible besides the use of the strip detector as a vertex one. For example, microchannel plates (MCPs) with a planar delay line were suggested for using as a vertex detector [17]. The use of a combination of the MCPs and the longitudinal strips with the planar delay line for recording an electron bunch could make it possible:

– to mark the triggering signal with a time resolution of about 0.1 ns;

– to achieve a spatial resolution of about 50 μm for one coordinate and 100–500 μm for other one.

To check this suggestion the recording efficiency for charged pions and protons with a momentum of 800 MeV/c was experimentally investigated using an assembly of two MCPs [17]. The standard plates MK – 34–10 made of lead glass with a channel density of 106 cm^{-2}, a thickness of 400 μm and a diameter of 34 mm were used. The 10–μm-dia channels were sloped at an angle of 10° to the slice axis.

The measured efficiency was (80±10)%, which allows the use of the MCP as a vertex detector of long-range particles in the AMPIR spectrometer. A thin-walled target (hydrogen or deuterium) which does not practically injected any unwanted mixture is placed and aligned inside the vertex detector. Besides the target itself the cryogenic target unit contains 1.5–m–long feed pipes and a vacuum cryogenic system used for the recondensation of liquid hydrogen (deuterium) by liquid helium. The cryogenic target unit is attached to the exit part of the vacuum tube separately from the attachment of the vertex detector so that the whole unit could be replaced by a foil target unit.

The inner vessel of the cryogenic target. (Fig.4) is made of 100–μm-thick aluminized mylar film in the form of a cylinder having an axis parallel to the beam and spherical bases. The vessel length is 10 mm, its diameter being 45 mm.

The beam focus is proposed to be at a distance of 25 mm from the inlet base. The minimum amount of the target wall substance, less than 100 μm mylar film, is within a particle exit angle range of 20°–145°, at the beam entrance (an entrance window diameter of 35 mm) and at the beam exit (an exit window diameter of 24 mm). The vessel is enclosed by a thermal scree of 12–μm–thick mylar film.

The target is filled with liquid hydrogen or deuterium. These working gases are liquified by liquid helium using liquid evaporation heat as well as gas heat content. Recondensation of the evaporated liquid proceeds automatically, the designed pressure in the target maintained with an accuracy of 0.05 atm. The 100 ℓ liquid helium vessel can ensure the continuous work of the target during four days. A special automation rack is provided to control and support the operation conditions of the cryostat.

During its exposure the target is inside the vacuum tube where for the normal operation conditions to be ensured vacuum must be better than 5.10 mm Hg. The distance from the centre of the target to the recondense is 2 m, which results in somewhat increased flow rate of helium as compared with that for small-volume targets. The amount of liquid helium in the dewar is determined by a superconducting level indicator.

A special vacuum casing conforming to the inner geometry of the vacuum tube was manufactured to perform cryogenic and vacuum tests. The cryogenic tests yielded that the target is filled by liquid hydrogen for 1 hour 40 min., the flow rate of liquid helium under steady–state conditions is 1l/h and the insulation vacuum in the end of 4-day operation is 3.10 mm Hg.

It is planned to use the optoelectrical methods to control the positions of the cryogenic and solid targets.

At present the beam pipe has been manufactured, the cryogenic target has been manufactured and tested, the assembly of solid targets has been designed and manufactured, the vertex detector has been designed.

2.4. Drift chamber

A cylindrical drift chamber with a three–dimensional readout of information is used as a central position detector in the spectrometer. The central wires stretched in the chamber along the axis of the vacuum tube record secondary charged particles escaping from a target at angles from 20° to 135°. The signals are read out from both wire ends. A distance from a track to a sense wire is determined from the time of drift electron arrival and a distance along the wire – from a ratio of amplitudes from the left and right ends (charge-devision method). These data and the value for magnetic field strength are used to calculate a particle momentum. With the momentum and the overall amplitude of the signal which is proportional to energy loss a type of particle can be determined by the dE/dx method. The direction of the particle's trajectory rotation in the magnetic field allows a sign of its charge to be determined.

The drift chamber is placed between the ion guide and the cryostat and consists of two parts: an internal chamber 340 mm in diameter and 600 mm long with 72 sense wire and an external chamber 960 mm in diameter and 1000 mm long with 360 sense wires.. The sense wires have a diameter of 15 μm and are made of W–Re (Au) alloy. In addition to the sense wires the internal (external) chamber contains 156(756) field and 84(394) potential and guard wires of beryllium bronze 100 and 200 μm in diameter. These wires are used to form an electric field having a strength of order of 1 kV/cm, whose map was preliminarily calculated. The calculation was based on the principle of minimization of the wire potentials with the simultaneous equalization of the charges on the sense wires to produce the uniform electric field inside the chamber (constant longitudinal strength and zero transversal one). The calculation was made for one layer in the chamber with allowance for the effect of other layers.

To secure the wires and fix their positions with an accuracy of $\sim$ 15 μm special plates with precise slots and contact units to read out signals and to supply potentials were designed. The total tension force for the wires is 500 kg. The sense wires are distributed along the chamber radius in three layers, each containing 12, 24 and 36 sectors respectively. Each sector includes 6 sense wires. In this way the track of a particle escaping from the target at an angle to the chamber axis can be recorded in 18 points. A particle emitted at an angle of $20^\circ < \theta < 30^\circ$ will be recorded at least in 12 points. To avoid the right-left ambiguity in restoring the particle track the sense wires are displaced by 200 μm from a plane passing through the potential wires of each sector. The maximum drift length for electrons is 40 mm.

The surface of the external chamber is covered by 36 scintillation plates used to record particles coming from the target and, together with the vertex detector, to trigger the chamber. The drift chamber is enclosed in a gastight box 1000 mm in diameter and 1600 mm long. Pipes brought out from the box rest on the frame of the magnet yoke. It is assumed to work under conditions of lowing down with a 90%Ar + 10%CO_2 gas mixture.

The feasibility of the drift chamber parameters presented in section 1.1 is borne out by the results of simulations and measurements carried out at several prototype chambers, both internal and external, with the use of π–meson beams, redioactive sources and cosmic–ray particles. Some of these results are given below.

The operation of the drift chamber within one sector was simulated with the use of GARFIELD program [18]. Figure 5 shows the equipotential lines obtained for a pre–optimized set of voltages. The field uniformity is seen to be sufficiently good. The drift lines from the track passing near the field wires are presented in Fig. 6a. It is readily seen that essentially the whole sector area is working. The drift lines

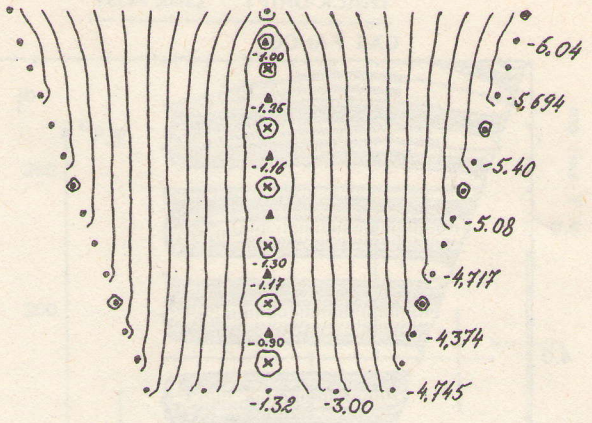

Fig. 5. The equipotential lines in the drift chamber sector from the GARFIELD calculations.

with allowance for a magnetic field of 10kG are shown in Fig. 6b (Lorentz angle is 17°). This series of calculations has indicated also a linearity of the first electron arrival time as a function of the distance from the sense wire (except a small area about 3 mm in size near the wire) and an independence of the electron drift velocity from the wire number as well as has simulated a signal shape (rise time, total duration and amplitude) agreeing well with that obtained experimentally.

To estimate the expected momentum and spatial resolutions of the drift chamber as well as the accuracy in restoring an interaction vertex the passage of a charged particle through the drift chamber with a 10 kG magnetic field was simulated. For this purpose a track was drawn with a prescribed momentum P and a given polar angle through a geometrically similar model of the chamber and the ideal points of intersection of the track with each of 18 sence wires were calculated. Then the positions of the calculated points were varied with given $\sigma_{\rho,\psi}$ and σ_z (the coordinate Z along the wire is unambiguously connected with the angle) according to the Gause law. The new displaced points were used to restore a new track position in the chamber and the corresponding change in the momentum.. Repeating this operation sufficient times one can obtain the P and distributions for prescribed values of these quantities as well as estimate the accuracy in restoring an interaction vertex. As a result of playing out 5000 events per each value of momentum and angle it was found that within an angle range of $20^\circ - 80^\circ$ $\Delta p/p$ (disregarding a multiple scattering) does not exceed 1%. The interaction vertex is restored in the plane ρ,φ with an accuracy better than 2.5 mm.

The possible momentum resolution was calculated with allowance for multiple scattering. The results obtained and the parameters used are given in Fig. 7.

The preliminary experimental verification of the drift chamber serviceability was made during long–term exposure of its module to hard cosmic rays. The

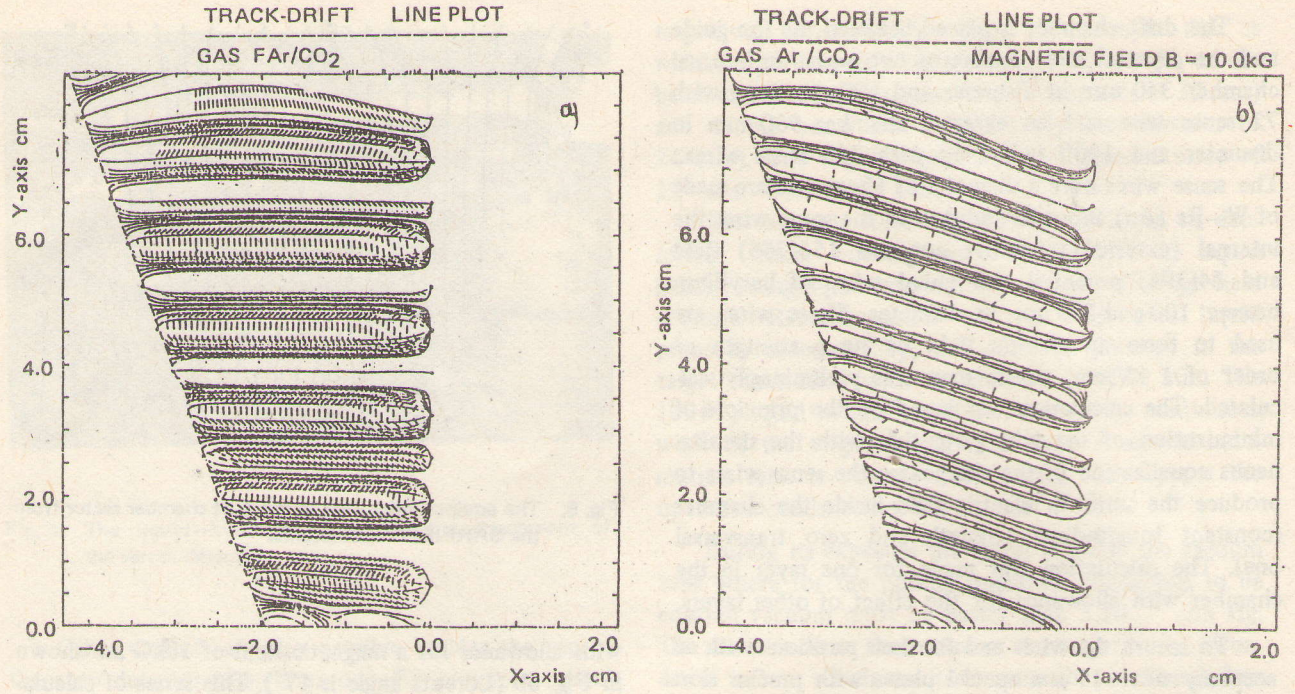

Fig. 6. The electron drift lines in the drift chamber sector without magnetic firld (a) and with a 10 kG magnetic field (b).

time and amplitude information was read out from six and three wires, respectively. The chamber was triggered by a system of scintillation counters. 90% Ar + 10% CO_2 mixture was used a working gas. Gases were cleaned from electronegative impurities (oxygen, water vapor, etc.) by a system of filters. On the whole, 65000 useful events were played out for various voltages at the field and potential wires. The drift velocity was determined from the distance between the peaks in the spectrum of a quantity $T = (t1 + t3)/2 - t2$ for the staggered wires (see Fig. 8).

For voltages at the field wires $U_{field} = -6.0$ kV and the potential wires $U_{pot} = -1.15$ kV the following basic results were obtained:

1) The efficiency $\eta = (98 \pm 1)\%$ remains constant along the wire length, is independent of the potential wire voltage in the range of 1.1–1.35 kV and weakly (less than 5%) decreases with the drift distance;

2) The mean ρ, φ–resolution at a drift length 2.5 to 20 mm is $\sigma_{\rho,\varphi} = (170 \pm 15)\ \mu m$ (see Fig. 9);

3) The Z–resolution for the vertical tracks in the central region is constant to be $\sigma_z = 2$ mm (Fig. 10) and grows at the wire edges up to 5 mm; which can be evidently attributed to the distortion of the electric field by the dielectrical ends of the chamber and can be suppressed by applying a correcting potential. The mean σ_z for all tracks $< \sigma_z > = 7$ mm.

The measurement of the parameters of a 600–mm–long prototype internal chamber showed that for 80% Ar + 20% CO_2 gas mixture at $U_{field} = -6.4$ kV and $U_{pot} = -1.7$ kV the ρ, φ – resolution follows well the formula $\sigma^2_{\rho,\varphi} = \sigma^2_0 + \sigma^2_D \cdot \chi_D$, where

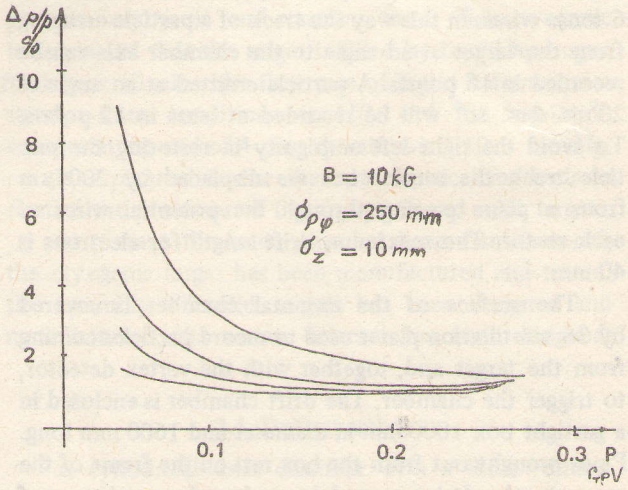

Fig. 7. The pulse resolution of the drift chamber for a 10 kG magnetic field, $\sigma_{\rho\varphi} = 250\ \mu m$ and $\sigma_z = 5$ mm.

χ_D is the drift distance;

$\sigma_0 = (63 \pm 41)\mu m$ and $\sigma_D = (168 \pm 8)\mu m$ (Fig. 11).

It follows from the calculated and measured results in total that the proposed design of the drift chamber meets the requirements, which are needed to implement the physical program outlined. At present the technical design of the drift chamber is over and its manufacturing has been started.

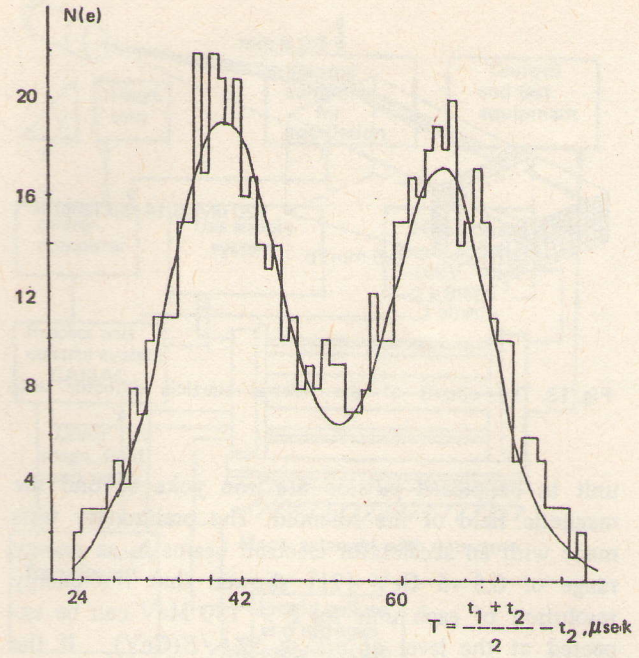

Fig. 8. The values of the function T = (t1 + t3)/2 – t2, where ti is the arrival time of the drift electrons at the i-th wire.

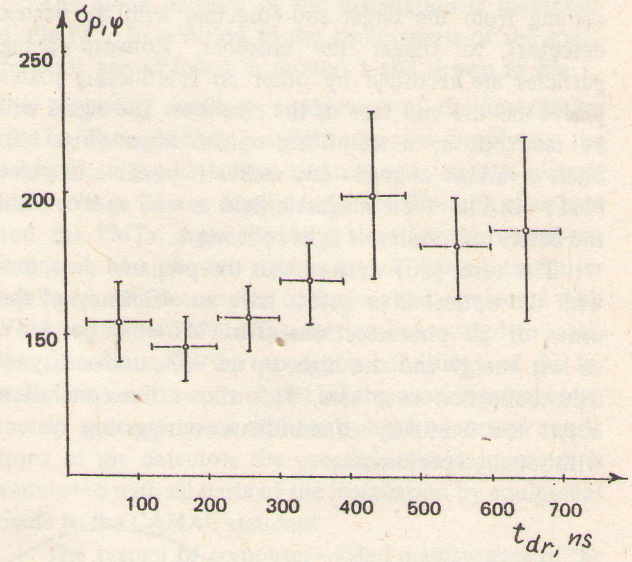

Fig. 9. The spatial resolution of the prototype drift chamber for 90%Ar + 10%Co2 gas mixture.

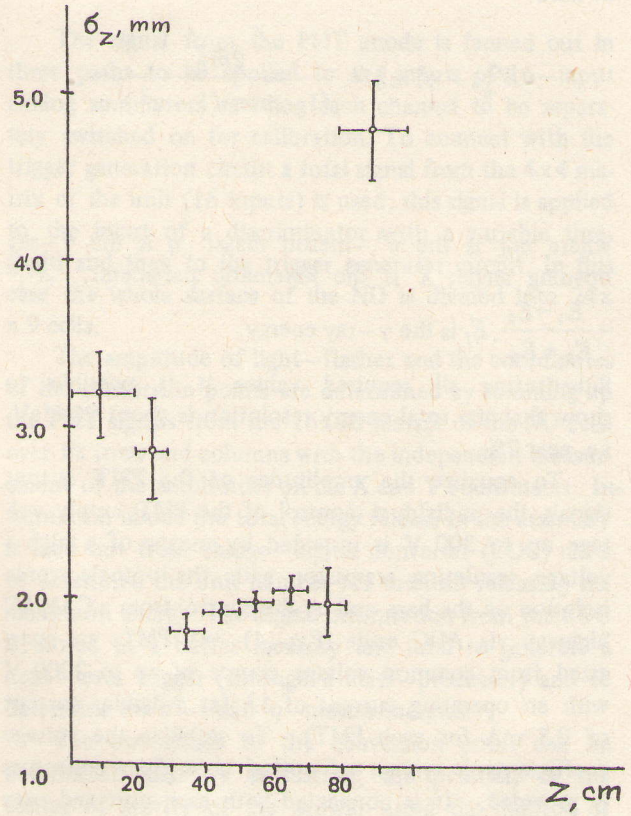

Fig. 10. The spatial resolution of Z-coordinate.

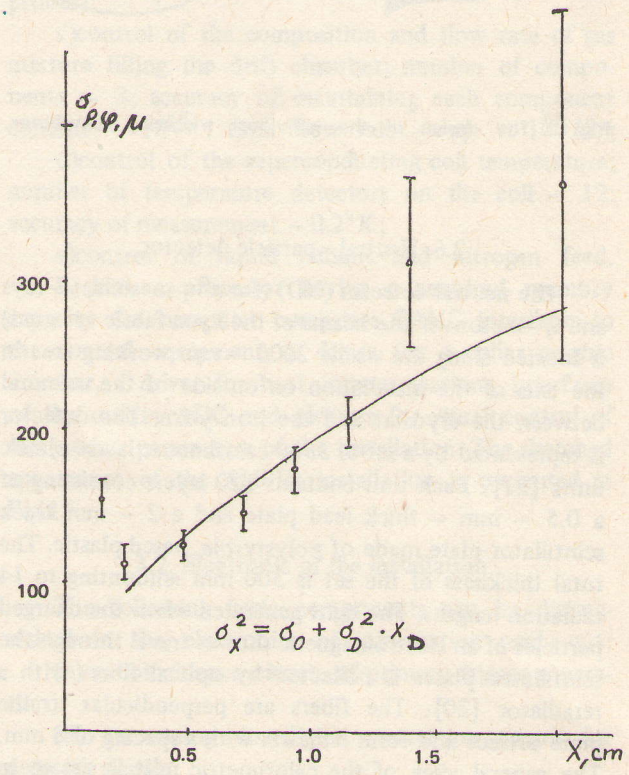

Fig. 11. The spatial resolution of the prototype drift chamber for 80%Ar + 20%Co2 gas mixture.

2.5. Triggering scintillators

The side surface of the external chamber is covered by 36 planar scintillating plates used to record particles coming from the target and (together with the vertex detector) to trigger the chamber. Forward–going particles are recorded by other 36 scintillating plates placed on the end face of the chamber. The signal will be read out by a reemitting optical fibers (Fig. 12). Such a variant of read–out makes it possible to place PMTs outside of the magnetic field as well as to ensure the better uniformity of light collection.

The tests [20] showed that the prepared detectors with the optical fiber guides have an efficiency of the order of 20 photoelectrons (for PMT–84) per MeV of lost energy and the high, up to 95%, uniformity of light collection over area. This allows the conclusion about the feasibility of scintillation triggering system with required performance.

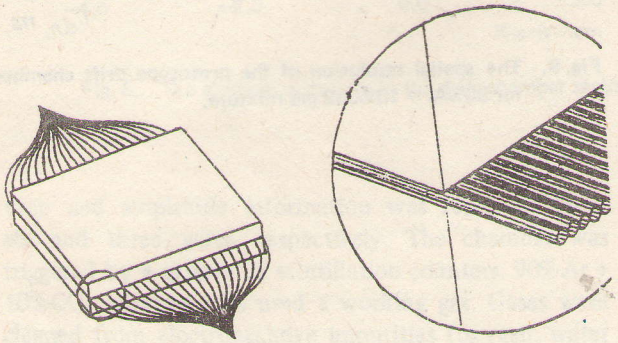

Fig. 12. The design of the individual triggering scintillator.

2.6. Neutral–particle detector

The neutral detector (ND) (for π^0 –mesons, γ–rays and η–mesons if the beams of the kaon fabric are used) is located along the whole 2000 – mm working area in the axis of the installation on outside of the solenoid between the cryostat and the iron yoke. The detector is represented by a set of 3360 calorimetric lead–plastic units [21]. Each unit contains 120 layers consisting of a 0.5 – mm – thick lead plate and a 2 – mm thick scintillator plate made of polystyrole based plastic. The total thickness of the set is 300 mm amounting to 14 radiation lengths. The light generated when the charged particles of an electromagnetic shower travel through the scintillator plates is collected by optical fibers with a reradiator [20]. The fibers are perpendicular to the plate surface and form a matrix with a spacing of 8 mm. The general view of the calorimetric unit is shown in Fig. 13.

The attenuation length for reradiated light in the fiber is about 150 cm (at a wavelength of 530 nm), which allows the photomultipliers looking over each

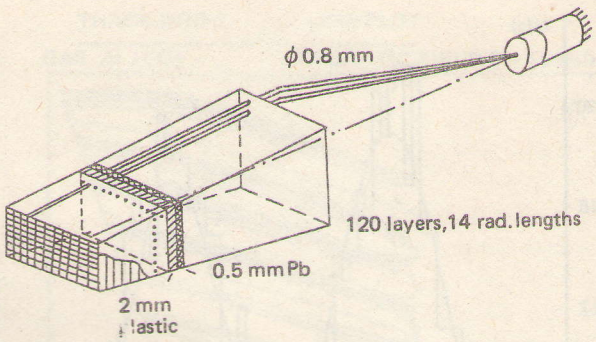

Fig. 13. The circuit of the neutral–particle detector unit.

unit to be placed putside the iron yoke beyond the magnetic field of the solenoid. The preliminary tests made with an accelerator electron beams in an energy range of 0.5–5 GeV [21] showed that the energy resolution of each unit for $E > 150$ MeV can be expected at the level of $\sigma/E \cong 5\%/\sqrt{E(\text{GeV})}$. If the coordinate of the point of γ – ray arrival in the ND volume is measured by extablishing which unit is triggered with a maximum signal amplitude, then the angular accuracy is 0.05 rad.

To estimate the possible energy resolution of the ND in recording to decay of a π^0 –meson with a kinetic energy of about 300 MeV the following formula can be used:

$$W^2_{\pi^0} = \gamma^2 m_0^2 = \frac{2m_0^2}{(1-\cos\eta)(1-x^2)}$$

where m_0 is the π^0–meson mass; η is the γ–ray opening angle; X is the kinematic parameter, $X = \frac{E_1-E_2}{E_1+E_2}$, E_i is the γ–ray energy.

Substituting all required values it is possible to show that the total energy resolution is about 20 MeV, i.e. near 7%.

To equalize the amplitudes of the PMT output signals the individual control of the PMT supply voltage up to 300 V is provided by means of a high–voltage regulating transistor with the optoelectronic isolation on the base and by the control from a CAMAC highway via ADC unite (Fig. 14). All PMTs are energized from common voltage cource of up to 2000 V with an operating current of 1A (at a divider current of 0.3 mA for each PMT). To stabilize the voltage coefficients a system of optical glass fiber collectors is provided. It is connected with each unit and uses light–emiting diodes as sources of light flashes with a pulse duration of 60 ns. The flash amplitude is selected by a separate reference PMT stabilized with the use of ^{137}Cs γ-ray sources and CsJ(Na) crystals.

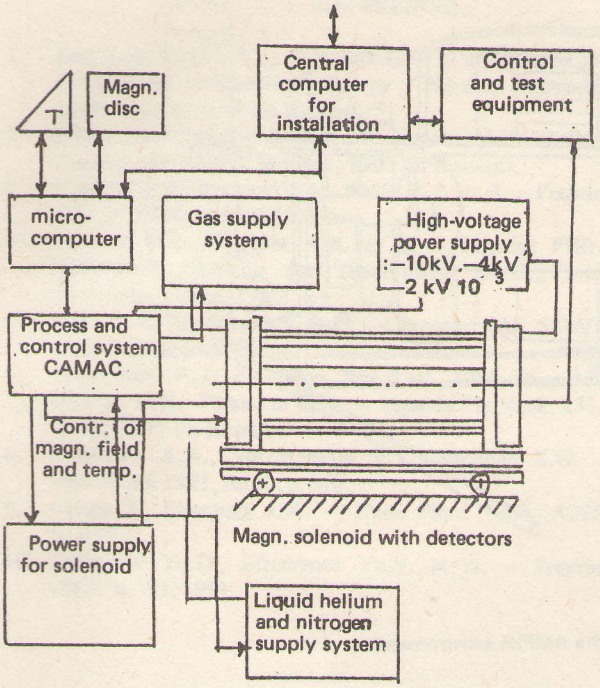

Fig. 14. The block diagram of the AMPIR spectrometer.

The signal from the PMT anode is fanned out in three paths to be applied to the inputs of 16-input analog summators enabling each channel to be separately switched on for calibration. To connect with the trigger generation circuit a total signal from the 4x4 matrix of the unit (16 inputs) is used; this signal is applied to the input of a discriminator with a variable threshold and then to the trigger generator circuit. In this case the whole surface of the ND is divided into 24x x 9 cells.

The amplitude of light-flashes and the coordinates of the conversion points are determined ay summing up the PMT signals from the 16x16 matrix of the ND cells over its rows and columns with the independent measurement of the amplitudes on the X and Y coordinates. Information about the total energy release in the assembly is read out from charge-digital converter (CDC) units to determine the unit number for the unit releasing the maximum energy. The digital information from the CDC is stored in a buffer memory and used to generate a next-level trigger (through a mass-processor) and to determine the π^0 - and η-meson energies.

The coordinate of the conversion point can be determined also by calculating the position of the center of gravity of the shower using the method of plotting the avalanche profiles along the X and Y coordinates. The spatial accuracy can be expected to be about 8 mm, which leads to a π^0-meson energy resolution of about 10 MeV. ($\cong$ 3%).

3. Control and read out of information

3.1. The block diagram of the AMPIR spectrometer

The block diagram of the installation is presented in Fig.14. In addition to the components of the spectrometer per se listed in section 1 and shown in Fig. 1, the following auxiliary equipment of the installation can be distinguished: a stabilized power supply for the solenoid, a liquid helium and nitrogen supply system, high-voltage power supply units for the drift chambers and the PMTs, a gas supply system for the chambers, and test and control equipment. A special computer equipped with a complex of devices and connected with a host computer of the installation is provided to maintain automatically the operation conditions of the installation, and to control and set the process parameters.

In order to check and control the operation conditions of the detectors the process control computer is connected with all parts of the installation by equipment made to the CAMAC standard.

The system of computer-aided maintenance of the installation operation conditions solves the following basic tasks:

a)control and stabilization of the drift chamber; high-voltage power supply; number of control channels - 63; required accuracy - 10^{-3} ;

b)control of the solenoid power supply; operating current - up to 3000A; accuracy of current setting - 10^{-3} ; number of measurement channels - 12 (Hall probes);

c)control of the composition and flow rate of gas mixture filling the drift chamber; number of components - 3; accuracy of maintaining each component content - 10^{-2} ; total flow rate - up to 100 l/h;

d)control of the superconducting coil temperature; number of temperature detectors on the coil - 12; accuracy of measurement - 0.2°K;

e)control of liquid helium and nitrogen feed.

Besides a processor having a required memory capacity the computer comprises CAMC interfaces to the control equipment, a driver for a collar graghic monitor, a driver for host communications, interfaces of the matrix ADC and plotters for visual control of the process parameters of the installation. The sketched appearance of the AMPIR installation is presented in Fig.15.

3.2. Electronic of the installation

The following basic components can be distinguished in the electronics of information read-out:

(a) a coincidence circuit of primary trigger generation;

(b) an analog-to-digital conversion circuit for detector signals;

(c) a primary selection system on the basis of programmable processor units;

(d) a processor for final selection of events from the background;

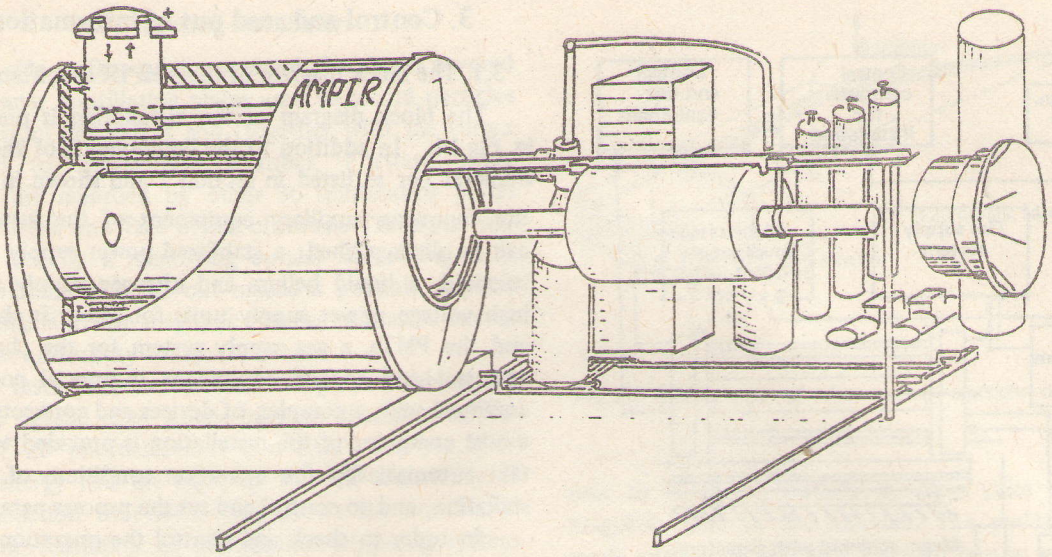

Fig. 15. The appearance of the AMPIR spectrometer.

(e) a buffer RAM to store the selected events;

(f) a host computer of the installation with a 9–Mbyte RAM.

Consider the electronics operation in more detail (using the reaction with emission of two pions as an example). The simultaneous arrival of signals from two of 36 scintillation plates is the condition of triggering in measuring the reaction with emission of two charged particles. In this case it is necessary also that two strips (from the total of 432) of the vertex detector would operate within a specified time gate. If the above requirements are met, a triggering pulse will be generated for the reading–out of information from the drift chamber and its conversion to the digital form. The signal from the output of the drift chamber amplifiers is applied upon being fanned out to a coder to determine the operated wire number and to the analog-to-digital conversion circuit.

The pulse from the trigger organization circuit is applied to a one–shot multivibrator to generate a time gate for a TDC. The time gate width is determined by the maximum drift time. Simultaneously the operation of both the coincidence circuit of event election and the trigger generation circuit is forbidden. At the same time the TDCs for the drift chambers is driven. The pulses from the drivers of the drift chambers serve as a stop signal for the TDC. These pulses trigger also the ADC gate generation circuits for the measurement of the amplitudes of signals from the wires required to measure dE/dx of an ionizing particle along its track and the Z–coordinate of the wires. Simultaneously a flag denoting the presence of information for the selection circuit is formed. During the conversion in the ADCs the inhibiting signals are generated for the inputs of the ADCs and the circuit determining the operated wire and strip numbers. The digitized information is written in the RAM. The word length per event corresponding to the passage of two charge particles through the detector volume within a specified time gate is 1500 bits. The digitization time

$$t = t_{\text{drift}} + t_{\text{coading}} + t_{\text{RAMwirting}} = 10\ \mu\text{s}$$

The primary selection of the events occurs by restoring the particle tracks in the volume of the drift chamber by a specified algorithm with the subsequent check of their compliance with the initial conditions of particle emission at one point of the target. The check is carried out by the superposition of the pre–calculated event mask complying with this criterion on the RAM content. To check the compliance of the kinematics with the chosen reaction the selected information about the events is processed by a program processor which restores the kinematics of events with allowance for the longitudinal and transversal momenta of the emitted particles as well as by the dE/dx method. The processed information is sent to the host computer where it is displayed and recorded on tape.

In conclusion it should be noted that, though the AMPIR spectrometer is conceptually close to the detectors used with colliding beams, its design features give hope for its isefulness in the intermediate–energy physics, in particular, for the use with the pion beams of meson factories and the photon beams of electron storage facilities. One can expect that new useful data on the nuclear structure, the mechanisms of the pion–nuclear and photonuclear reactions, the role of pion-nucleon degrees of freedom in a nucleus and other properties of nuclear matter could be obtained with the AMPIR spectrometer.

REFERENCES

1. Esin S.K., Kvasha A.I., Kravchuk L.V. et al. Proc. of Int. Seminar on Intermediate–Energy Physics, Noivember 1989, Moscow, p.18 (in Russian).
2. Belyaev S.T., Gurevich G.M., Nedorezov V.G. et al. – Preprint IAE 5046/2, Moscow, 1990 (in Russian).
3. Kurepin A.B., Krasnov V.A., Berlev A.I. et al. – Preprint INR, P–0484, 1986 (in Russian).
4. Krasnov V.A., Kurepin A.B. et al. – Preprint FUB–HEP/90–21, Institut fur Theoretische Physik Freine Universitat, Berlin, 1990.
5. Mukhin K.N., Patarakin O.O. – Preprint IAE 5276/2, 1990 (in Russian).
6. Donoghue J.F. et al. – Phys. Rev. Lett., 1984, 53, p.747.
7. Mukhin K.N., Patarakin O.O. – Uspekhi Fiz.Nauk, 133, 1981, p.377 (in Russian).
8. Bolokhov A.A., Vereshchagin V.V., Sherman S.G. – Nucl. Phys. 1991, A530, p.660.
9. Cohen J., Eisenberg J.M. – Nucl. Phys. 1983, A395, p.. 389.
10. Bahyukov Yu.D., Efremenco Yu.V. et al. – Preprint ITER 4–91, 1991.
11. Kurepin A.B. – Nucl. Phys. A519, 1990, p.395c.
12. Golubeva M.B. et al. – JETP Lett., 51, 1990, p.298 (in Russian).
13. Miller G.A. – Phys. Rev. 1984, 53, p. 2008.
14. Green M.C. et al. – Bull. Am. Phys. Soc., 1982, 27, p.468.
15. Krasnov V.A., Kurepin A.V., Reshetin A.I. Phys.Lett. 1982, 1088, p.11.
16. Bonner B.E. et al. Phys. rev., 1978, C18, p. 1418.
17. Gordon Research Conf. on Photonuclear Reactions – 1990.
18. Goble R.L., Rosenfeld R., Rosner J.L. - Phys. Rev. D, 1989, 39, 3264.
19. Valiev F.F., Feorilov G.A., Tsvinev A.P., et al. – JINR Rapid communic. No. 4[50] –91.
20. Veenhof R., GARFIELD, A Drift Chamber Simulation Program, HELIOS No.154, 1986.
21. Berlev A.I., Krasnov V.A., Kovinsky V.I. et al. NIM A283, 1989, p.614.
22. Gladyshev V.A., Golubeva M.B., Goncharenko O.N. et al. – JINR Rapid Communications No.2[48] –91; p.39.
23. Atayan G.S., Gladyshev V.A., Gnidenko et al. Preprint INR–736/91, 1991.